Underwater Ultrasonic Topological Waveguides by Metal Additive Manufacturing

Michael Y Wang,[1] Mythili Thevamaran,[2] Michael Sabatini Mattei,[3] Brandon G Hacha,[3] Gerardo Mazzei Capote,[4] Zongfu Yu,[1] Tim Osswald,[4] Randall H Goldsmith,[3] Dan Thoma,[2] and Chu Ma[1]

[1)]*Department of Electrical and Computer Engineering, University of Wisconsin-Madison*

[2)]*Department of Materials Science and Engineering, University of Wisconsin-Madison*

[3)]*Department of Chemistry, University of Wisconsin-Madison*

[4)]*Department of Mechanical Engineering, University of Wisconsin-Madison*

(*Electronic mail: chu.ma@wisc.edu)

Acoustic topological systems provide a new route to explore novel wave properties and wave manipulation capabilities. Currently, most of the experimentally demonstrated acoustic topological systems are for airborne acoustic waves, and work at or below the kHz frequency range. Here, we report an underwater acoustic topological waveguide that works at the MHz frequency range. The 2D topological waveguide was formed at the interface of two hexagonal lattices with different pillar radii that were fabricated with metal additive manufacturing. We demonstrated the existence of edge stages both numerically and in underwater experiments. Our work has potential applications in underwater/biomedical sensing, energy transport, and acoustofluidics.

Topological insulators possess properties originating in the quantum spin Hall effect, a major area of interest in condensed matter physics[1,2]. The unique conduction of electrons on the edges instead of the bulk of condensed materials in a topological insulator was first discovered in electronic materials. With insensitivity of the edge states to defects, topological insulators possess a huge potential for energy and information transport with high efficiency[1]. Such unique properties are attributed to the intrinsic spin -1/2 fermionic character of electrons.

Topological insulators are also realized in bosonic systems, such as photonic materials and acoustic materials by exploiting the pseudo-spin states in those materials[3–32]. In photonic materials, the pseudo-spin states in topological insulators are realized by generating photon polarization states either by symmetry breaking or permittivity/permeability matching[3–7,27]. An active area is use of new designs and materials to achieve the required refractive index contrast[33,34]. Acoustic systems, especially longitudinal airborne or underwater acoustic systems, do not have polarization states. Instead, the pseudo-spin states are generated by constructing degenerate artificial acoustic spin-1/2 states based on breaking time-reversal symmetry[8–12,15,16,18,28,31,32,35], zone-folding[8,12,35], accidental degeneracy[20,23], coupled resonators and waveguides[13,16,21,23,29], and valley pseudo-spin[19,22,24,30]. Fascinating ways to manipulate acoustic waves are demonstrated with acoustic topological insulators, for example, topologically robust and defect-insensitive wave guiding and splitting[8,9,11,28], directional acoustic signal transmittance and reception robust against surrounding noise and competing signals[22], negative refraction of topological surface waves[25], and negative refraction out-coupling into free space[24]. Those acoustic wave manipulation methods could provide new opportunities for acoustic wave manipulation, sensing and communication[8,22,26–31,35].

Currently, most of the experimentally demonstrated acoustic topological materials are for airborne acoustic waves at or below the kHz frequency range[9,10,12,16]. A few works detailing underwater acoustic topological materials are also in the kHz frequency range[11,30,31]. Underwater acoustic topological materials working in the MHz and higher frequency ranges that are most relevant to applications in biomedical ultrasound, acoustofluidics, and ultrasonic on-chip communication and signal processing have not been reported. The main reason for this gap is due to the difficulty in fabrication. Large acoustic impedance contrast between the constituent materials of the phononic crystals and the background medium is required in acoustic topological materials. This is easy to achieve with high-resolution 3D printing of polymers when the background medium is air. However, polymers do not have sufficient acoustic impedance contrast with water. Metals/ceramics could be promising candidates for underwater acoustic topological materials, yet

precise fabrication of metal/ceramic structures for the MHz frequency ranges is difficult.

In our study, we fill this gap by demonstrating an underwater 2D acoustic topological waveguide working in the MHz frequency range fabricated by metal 3D printing. We experimentally characterized the topological behavior through transmission spectra measurements and observed the corresponding topological states. Although 2D topological waveguides have been reported in THz and EM wave domains[36], our work opens the path for fabricating and characterizing acoustic topological materials in the MHz frequency range in water that will benefit a wide range of applications in biomedical ultrasound imaging, diagnosis, therapy, particle manipulation and drug delivery, as well as ultrasound on-chip communication and information processing[29,37].

The structure of the 2D acoustic topological waveguide is depicted in Figure 1a). The waveguide locates at the interface of two hexagonal lattices of metal rods that have C_{6v} symmetry. The lattice constant is a_0=0.83mm, and the radii of the rods on the two sides of the waveguide interface are *r/a*=0.32 and 0.41, respectively. The dispersion relations of the hexagonal lattices with the radii of *r/a*=0.41 and 0.32 are plotted in Figure 1b) and d), respectively, corresponding to the rods on the two sides of the waveguide interface. When the radius of the pillars in the hexagonal lattice is larger or smaller than *r/a*=0.3576, at which a double-Dirac-cone structure exists as shown in Figure 1c), the two two-fold degeneracy appears near the Γ point, forming band gaps. Analogous to electron orbitals, p_x, p_y, d_{xy} and $d_{x^2-y^2}$ refer to the 'acoustic orbitals' that defines the acoustic pressure distribution modes in a unit cell of the hexagonal lattice. When *r/a*=0.41, p_x and p_y orbitals are associated with lower energy bands, and the d_{xy} and $d_{x^2-y^2}$ are located at higher energy bands. When *r/a*=0.32, the p and d orbitals flipped. We call the lattice with *r/a*=0.41 the trivial lattice, and the one with *r/a*=0.32 the topological non-trivial lattice. The insets in Figure 1b) and d show the different orbitals associated with the band structures that confirm the band inversions at different *r/a* values.

At the interface between the two phononic lattices with *r/a*=0.32 and 0.41, the topological phase transition, which occurs due to the phase continuity and the flipped orbitals of phononic crystals on the two sides of the interface, creates edge stages inside the bulk band gap along the interface. We constructed a super lattice as showed in Figure 1e) that is formed by concatenation of a topological lattice and a trivial lattice. The top and bottom edges were selected as the periodic boundaries to obtain the band structure of the super lattice as plotted in Figure 1f). The symmetric mode (S) and anti-symmetric mode (A) originated from the hybridization of the p and d orbitals can be written as $S = (p_x + d_{x^2-y^2})/\sqrt{2}$ and $A = (p_y + d_{xy})/\sqrt{2}$. The acoustic pressure distributions of the

symmetric mode (S) and anti-symmetric mode (A) plotted in Figure 1e) are the mode distributions in the super lattice when $k_{||} = 0$ and at the frequency where the red line and the blue line crosses in Figure 1f). The S and A modes further hybridize to generate the acoustic spin-up edge states (S$+i$A = $p_+ + d_+$, red line in Figure 1f) and spin-down edge states (S$-i$A = $p_- + d_-$, blue line in Figure 1f), respectively.

We conduct numerical simulation of the acoustic wave transmission through the trivial lattice, topological lattice, and the waveguide that is formed at the interface between the trivial and topological lattices. Simulations are performed with COMSOL MULTIPHYSICS 5.6. The pillars are modeled as acoustically rigid structures.

To calculate the transmission spectra, we numerically construct the topological waveguide that is formed at the interface of the two hexagonal lattices with r/a= 0.32 and 0.41. A point monopole source is placed at the top of the trivial lattice, topological lattice, and the interface, respectively. The transmitted wave amplitudes are measured at the bottom of the lattices at the same horizontal positions as the incident source. Another simulation is conducted to measure the transmitted amplitude through an empty space having the same size as the lattice. The transmission spectra are calculated as the ratio between the transmitted amplitudes through the lattices and that through the empty space is given in Figure 2a). Both perfect lattice and lattice with defects were simulated. For the frequency range from 1.01MHz to 1.08MHz, the wave transmission through both the trivial and topological lattices are small because of the band gap. In contrast, a high transmission peak appears in the transmission spectrum of the waveguide in this frequency range resulting from the edge stage inside the bandgap.

The above mentioned simulations are performed in a 2D setting. We also constructed the 3D version of the 2D lattice with multiple pillar height h and calculated the transmission spectra at the interface, as shown in Figure 2c). When there is no thermal viscous loss in the simulation environment, the acoustic transmissions at the interface with multiple pillar heights are consistent with our 2D simulation and the pillar height does not influence the acoustic transmission through the topological waveguide. However in experiments, the thermal viscous loss will induce more attenuation in the transmission when the pillar height is smaller.

Compared to waveguides formed by hard walls, the topological waveguides is robust to defects in the waveguide structure. The broken pillars or additional scatterers in the topological lattice will not influence the overall wave transmission behavior[5,8,31,32,35], as shown in Figure 2b) (perfect lattice) and d) (lattice with defects) that demonstrate the acoustic wave distribution of the

edge stage at the interface at the frequency of 1.07MHz. We also plotted the acoustic transmission coefficients through the waveguide with and without defects in Figure 2a). The transmission coefficient through both the perfect lattice waveguide and the waveguide with defects are similar. Besides defects, the acoustic transmission will also be less influenced by the sharp bending in the waveguide compared to hard-wall waveguides[33,38].

In order to offer high acoustic impedance contrast with water and micrometer-scale geometric accuracy, Laser Powder Bed Fusion (LPBF) technology was used to 3D print metallic lattice structures. The height of the pillars was 8.6 mm (more than 6 times the acoustic wavelength underwater at 1.08 MHz) to make sure that the two-dimensional approximation is applicable. The intended diameters of the pillars were 270 and 340 μm. Boundary walls were constructed around the pillars to avoid the collision of the recoater with the pillars during the printing process. The structures were oriented at an angle of 30 degrees from X axis on the 25 cm $\times$ 25 cm $\times$ 10 cm build platform. A support structure (0.5 mm thick) was used in between the bottom plate of the pillars and build platform to dissipate the heat from the printed layers and assist in detaching the samples from the build platform.

A 400 W Ytterbium fiber laser with wavelength 1060 nm and beam diameter 100 μm was used for the LPBF processing. Argon gas was used as an inert gas to keep the oxygen content as low as 0.1% during printing to prevent oxidation. Gas atomized Haynes 282 powdered material with a particle size ranging from 15-40 μm was used. The process parameters used were laser power of 250 W, laser scanning speed of 1000 mm/s, layer thickness of 40 μm, and hatch distance of 0.11 mm[39].

The printing process provides relatively precise control of the lattice geometries. Only small surface roughness and slight bending of the rods toward varying directions are introduced by fabrication. Figure 3a) and b) shows the side view and top view of the printed topological waveguide lattice under a microscope. From Figure 3a) and our microscope measurements, the diameters of the pillars stays nearly a constant along the height direction. We also took over a hundred measurements of distances between the nearest pillars in the fabricated lattices, a_i, using a microscope as shown in Figure 3b), and the distribution of the measured a_i's is given in Figure 3c). Those values are averaged to get the effective lattice constant a as a=0.83 mm. This value is used in the simulations throughout the rest of the paper.

The schematic of the experimental setup is shown in Figure 4a). The transmitter, lattice sample and receiver are aligned along one axis. Both the transmitter and receiver are OLYMPUS V303-

SU. The surroundings of the sample are covered by metal plates. Two slits with the same height of the lattice and the width of 5 mm are cut from the metal plates, one at the transmitting side and one at the receiving side. The incident and transmitted waves can only pass through the slits. Figure 4b) gives a picture of the experimental setup, where the sample is mounted on the top of a post holder and the two slits are hung at two sides of the sample facing each other. The acoustic transmission through the trivial lattice, topological lattice, and the interface are measured by moving the two slits to the trivial side, topological side, and at the location of the interface, respectively. The received signals are analyzed via Keysight DSOX3024T oscilloscope and MATLAB.

The emitted signal is a five-period pulse with center frequency f_c. Two measurements are conducted for each center frequency f_c of the emitted pulse in order to get the acoustic wave transmission coefficient through the sample in the frequency range around the corresponding f_c. One measurement is obtained when the sample is placed in between the transmitter and the receiver, and a reference measurement is obtained when the sample is removed and the emitted pulse propagates through pure water between the transmitter and the receiver. An example of the received signal transmitted through the sample is shown in Figure 4c). The frequency spectrum of the transmission coefficient is calculated as the ratio of the spectrum amplitudes of the two measurements with and without the sample.

We set the center frequency f_c to 0.9 MHz, 1 MHz, and 1.1 MHz and obtain multiple frequency spectra of the transmission coefficient, as shown in Figure 4d). For each f_c, we choose the spectrum section between the full width at half maximum (FWHM) points around f_c, as illustrated by the shaded areas in Figure 4d), and set other spectrum sections to zero. The final transmission spectrum is obtained from the average of the transmission coefficient spectra with different f_c's. The above process is repeated at least 10 times and averaged to reduce the random noise from the instruments. The resulting transmission coefficients as a function of frequency are plotted in Figure 4f) for the topological lattice (r/a=0.32), trivial lattice (r/a=0.41), and the edge stage along the waveguide. The low transmission at and around 1.07 MHz through the trivial and the topological lattices indicates the band gaps. The edge stage along the waveguide is indicated by the 5 dB higher transmission coefficient at and around 1.07 MHz.

The magnitudes of the experimentally measured transmission coefficients (Figure 4f)) are strongly influenced by the damping of acoustic waves when transmitting through the closely packed pillar lattices, especially through the trivial lattice where the distance between the neighboring pillars is less than 20 μm. As a result, the difference between the transmission coefficient

at the edge state and that at the band gap is less obvious in experiment than in simulation. Moreover, the experimentally measured transmission coefficient vs. frequency curve of the topological lattice (r/a=0.32) is up-shifted by 0.05 MHz compared to in simulation, mainly because of the deformation of the metal pillars during 3D printing. The topological lattice has the pillar diameter of around 530 μm. Such thin pillars are more susceptible to bending deformation.

We designed, fabricated and experimentally characterized an MHz underwater ultrasound topological waveguide that opens the path towards exploring quantum behavior of classic acoustic systems at ultrasound frequencies in water/tissue. The topological waveguide was fabricated by metal 3D printing that gives enough acoustic impedance contrast with water and allows the control of geometric parameters of metallic structures with sub-millimeter resolution. Potential applications of topological waveguides include underwater acoustic energy transportation, sensing, communication, information processing, biomedical particle manipulation, and ultrasonic imaging.

This research was supported by the National Science Foundation through the University of Wisconsin Materials Research Science and Engineering Center (DMR-1720415). The additive manufacturing costs were supported by UW2020 WARF Discovery Institute Funds.

The data that support the findings of this study are available from the corresponding author upon reasonable request.

REFERENCES

[1]M. Z. Hasan and C. L. Kane, "Colloquium: topological insulators," Reviews of modern physics **82**, 3045 (2010).

[2]H. Ge, M. Yang, C. Ma, M.-H. Lu, Y.-F. Chen, N. Fang, and P. Sheng, "Breaking the barriers: advances in acoustic functional materials," National Science Review **5**, 159–182 (2018).

[3]A. B. Khanikaev, S. H. Mousavi, W.-K. Tse, M. Kargarian, A. H. MacDonald, and G. Shvets, "Photonic topological insulators," Nature materials **12**, 233–239 (2013).

[4]T. Ma, A. B. Khanikaev, S. H. Mousavi, and G. Shvets, "Guiding electromagnetic waves around sharp corners: topologically protected photonic transport in metawaveguides," Physical review letters **114**, 127401 (2015).

[5]L.-H. Wu and X. Hu, "Scheme for achieving a topological photonic crystal by using dielectric material," Physical review letters **114**, 223901 (2015).

[6]W.-J. Chen, S.-J. Jiang, X.-D. Chen, B. Zhu, L. Zhou, J.-W. Dong, and C. T. Chan, "Experi-

mental realization of photonic topological insulator in a uniaxial metacrystal waveguide," Nature communications **5**, 1–7 (2014).

[7]Y. Yang, Z. Gao, H. Xue, L. Zhang, M. He, Z. Yang, R. Singh, Y. Chong, B. Zhang, and H. Chen, "Realization of a three-dimensional photonic topological insulator," Nature **565**, 622–626 (2019).

[8]C. He, X. Ni, H. Ge, X.-C. Sun, Y.-B. Chen, M.-H. Lu, X.-P. Liu, and Y.-F. Chen, "Acoustic topological insulator and robust one-way sound transport," Nature physics **12**, 1124–1129 (2016).

[9]Z. Zhang, Q. Wei, Y. Cheng, T. Zhang, D. Wu, and X. Liu, "Topological creation of acoustic pseudospin multipoles in a flow-free symmetry-broken metamaterial lattice," Physical review letters **118**, 084303 (2017).

[10]J. Lu, C. Qiu, L. Ye, X. Fan, M. Ke, F. Zhang, and Z. Liu, "Observation of topological valley transport of sound in sonic crystals," Nature Physics **13**, 369–374 (2017).

[11]H. Dai, B. Xia, and D. Yu, "Temperature-controlled tunable underwater acoustic topological insulators," Journal of Applied Physics **125**, 235105 (2019).

[12]H. Dai, M. Qian, J. Jiao, B. Xia, and D. Yu, "Subwavelength acoustic topological edge states realized by zone folding and the role of boundaries selection," Journal of Applied Physics **124**, 175107 (2018).

[13]A. B. Khanikaev, R. Fleury, S. H. Mousavi, and A. Alu, "Topologically robust sound propagation in an angular-momentum-biased graphene-like resonator lattice," Nature communications **6**, 1–7 (2015).

[14]R. Fleury, D. L. Sounas, C. F. Sieck, M. R. Haberman, and A. Alù, "Sound isolation and giant linear nonreciprocity in a compact acoustic circulator," Science **343**, 516–519 (2014).

[15]X. Zhang, H.-X. Wang, Z.-K. Lin, Y. Tian, B. Xie, M.-H. Lu, Y.-F. Chen, and J.-H. Jiang, "Second-order topology and multidimensional topological transitions in sonic crystals," Nature Physics **15**, 582–588 (2019).

[16]H. Xue, Y. Yang, F. Gao, Y. Chong, and B. Zhang, "Acoustic higher-order topological insulator on a kagome lattice," Nature materials **18**, 108–112 (2019).

[17]K. Sakoda, "Double dirac cones in triangular-lattice metamaterials," Optics express **20**, 9925–9939 (2012).

[18]Z. Yu, Z. Ren, and J. Lee, "Phononic topological insulators based on six-petal holey silicon structures," Scientific reports **9**, 1–8 (2019).

[19]Y. Shen, C. Qiu, X. Cai, L. Ye, J. Lu, M. Ke, and Z. Liu, "Valley-projected edge modes observed in underwater sonic crystals," Applied Physics Letters **114**, 023501 (2019).

[20]Z.-G. Chen, X. Ni, Y. Wu, C. He, X.-C. Sun, L.-Y. Zheng, M.-H. Lu, and Y.-F. Chen, "Accidental degeneracy of double dirac cones in a phononic crystal," Scientific reports **4**, 1–7 (2014).

[21]A. Dutt, M. Minkov, I. A. Williamson, and S. Fan, "Higher-order topological insulators in synthetic dimensions," Light: Science & Applications **9**, 1–9 (2020).

[22]Z. Zhang, Y. Tian, Y. Wang, S. Gao, Y. Cheng, X. Liu, and J. Christensen, "Directional acoustic antennas based on valley-hall topological insulators," Advanced Materials **30**, 1803229 (2018).

[23]Z.-G. Chen and Y. Wu, "Tunable topological phononic crystals," Physical Review Applied **5**, 054021 (2016).

[24]Z. Zhu, X. Huang, J. Lu, M. Yan, F. Li, W. Deng, and Z. Liu, "Negative refraction and partition in acoustic valley materials of a square lattice," Physical Review Applied **12**, 024007 (2019).

[25]H. He, C. Qiu, L. Ye, X. Cai, X. Fan, M. Ke, F. Zhang, and Z. Liu, "Topological negative refraction of surface acoustic waves in a weyl phononic crystal," Nature **560**, 61–64 (2018).

[26]X. Zhang, M. Xiao, Y. Cheng, M.-H. Lu, and J. Christensen, "Topological sound," Communications Physics **1**, 1–13 (2018).

[27]M. Li, D. Zhirihin, M. Gorlach, X. Ni, D. Filonov, A. Slobozhanyuk, A. Alù, and A. B. Khanikaev, "Higher-order topological states in photonic kagome crystals with long-range interactions," Nature Photonics **14**, 89–94 (2020).

[28]X. Zhang, B.-Y. Xie, H.-F. Wang, X. Xu, Y. Tian, J.-H. Jiang, M.-H. Lu, and Y.-F. Chen, "Dimensional hierarchy of higher-order topology in three-dimensional sonic crystals," Nature communications **10**, 1–10 (2019).

[29]H. Dai, B. Xia, and D. Yu, "Microparticles separation using acoustic topological insulators," Applied Physics Letters **119**, 111601 (2021).

[30]S. Zheng, G. Duan, and B. Xia, "Underwater acoustic positioning based on valley-chirality locked beam of sonic system," International Journal of Mechanical Sciences **174**, 105463 (2020).

[31]S.-Y. Yu, C. He, Z. Wang, F.-K. Liu, X.-C. Sun, Z. Li, H.-Z. Lu, M.-H. Lu, X.-P. Liu, and Y.-F. Chen, "Elastic pseudospin transport for integratable topological phononic circuits," Nature communications **9**, 1–8 (2018).

[32]J. Mei, Z. Chen, and Y. Wu, "Pseudo-time-reversal symmetry and topological edge states in two-dimensional acoustic crystals," Scientific reports **6**, 1–7 (2016).

[33]M. Sabatini Mattei, B. Liu, G. A. Mazzei Capote, Z. Liu, B. G. Hacha, T. A. Osswald, Z. Yu,

and R. H. Goldsmith, "3d printed polymer photonic topological insulators and their robustness to fabrication disorder," ChemRxiv (2022), 10.33774/chemrxiv-2021-7d3xh-v2.

[34]G. A. Mazzei Capote, M. C. Montoya-Ospina, Z. Liu, M. S. Mattei, B. Liu, A. P. Delgado, Z. Yu, R. H. Goldsmith, and T. A. Osswald, "Compounding a high dielectric constant thermoplastic material for production of microwave photonic crystals through additive manufacturing," ChemRxiv (2021), 10.26434/chemrxiv-2021-gmm4l.

[35]Z.-D. Zhang, S.-Y. Yu, H. Ge, J.-Q. Wang, H.-F. Wang, K.-F. Liu, T. Wu, C. He, M.-H. Lu, and Y.-F. Chen, "Topological surface acoustic waves," Physical Review Applied **16**, 044008 (2021).

[36]M. T. A. Khan, H. Li, N. N. M. Duong, A. Blanco-Redondo, and S. Atakaramians, "3d-printed terahertz topological waveguides," Advanced Materials Technologies **6**, 2100252 (2021).

[37]R. H. Olsson III and I. El-Kady, "Microfabricated phononic crystal devices and applications," Measurement science and technology **20**, 012002 (2008).

[38]Z. Zhang, Y. Tian, Y. Cheng, Q. Wei, X. Liu, and J. Christensen, "Topological acoustic delay line," Physical Review Applied **9**, 034032 (2018).

[39]Z. Islam, A. K. Agrawal, B. Rankouhi, C. Magnin, M. H. Anderson, F. E. Pfefferkorn, and D. J. Thoma, "A high-throughput method to define additive manufacturing process parameters: Application to haynes 282," Metallurgical and Materials Transactions A **53**, 250–263 (2022).

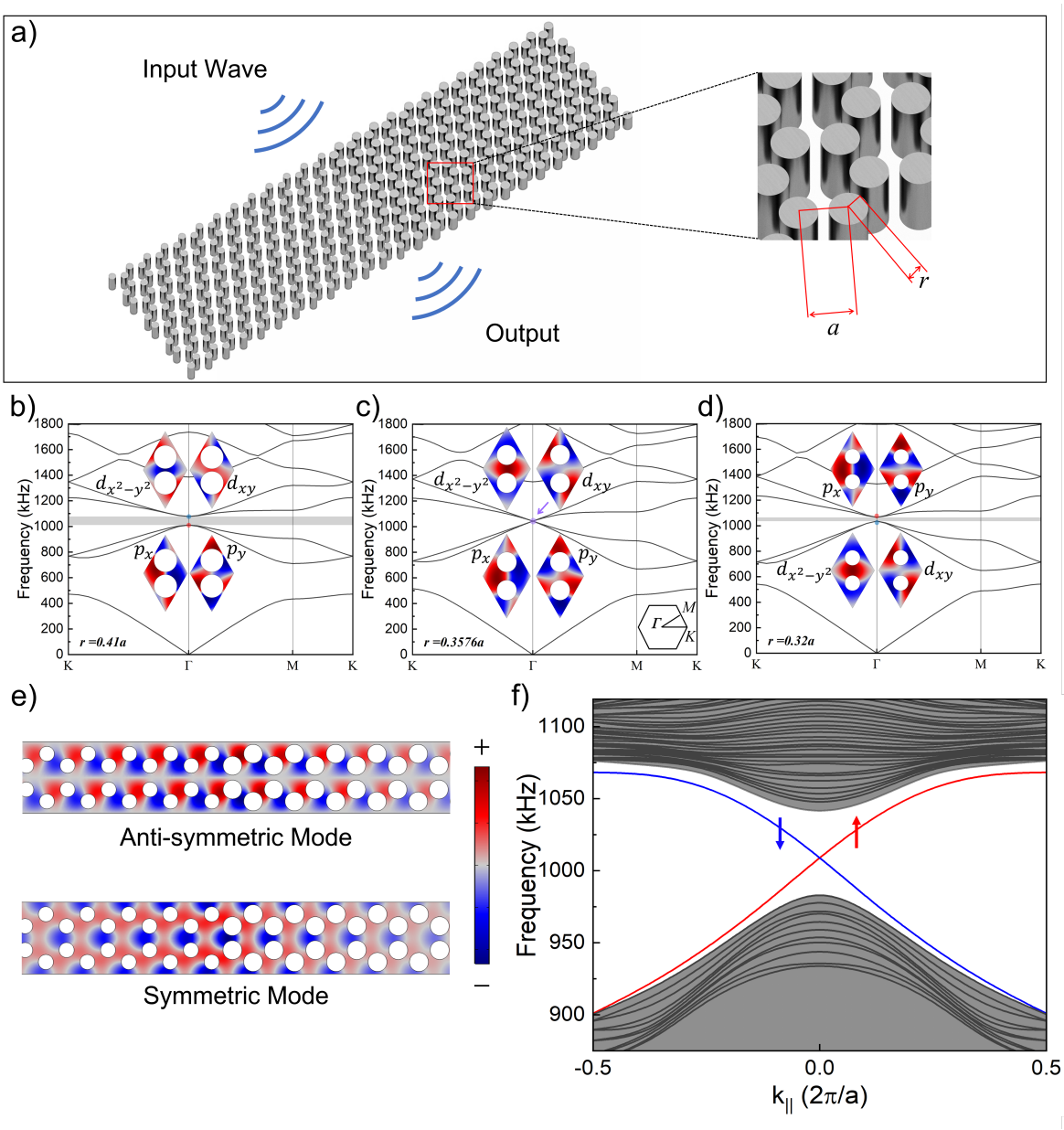

FIG. 1. a) A schematic of the topological waveguide constructed at the interface of two types of phononic lattices with the same lattice constant a but different radii r for metal pillars. b), c) and d) are the dispersion relations of the phononic lattices with the filling ratio of r/a=0.41, 0.3576 and 0.32, respectively. The inset shows the different acoustic states p_x, p_y, d_{xy}, and $d_{x^2-y^2}$. The dispersion relation with the filling ratio of r/a=0.3576 has a four-fold degenerate Dirac cone. e) A super lattice formed by the concatenation of a trivial lattice and a topological lattices, and the acoustic pressure distribution of the anti-symmetric mode (A) and symmetric mode (S) in the super lattice. e) The dispersion relation of the super lattice. The shadowed area represents the bulk states. The red and blue lines in the band gap represent acoustic spin-up and spin-down edge states.

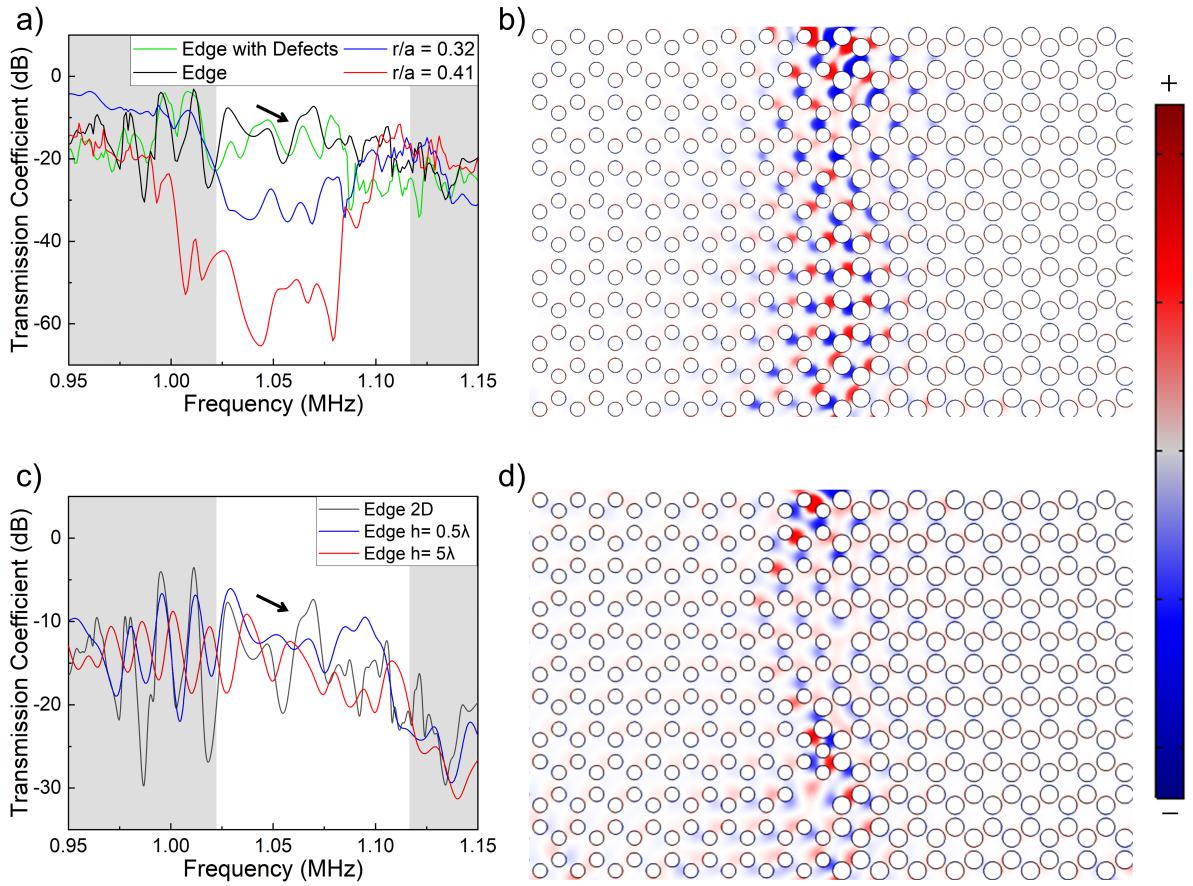

FIG. 2. a) and c) are calculated transmission spectra. The black, green, blue and red curves in a) represent the transmission coefficient spectrum along the waveguide formed by perfect lattice, waveguide formed by lattice with defects, and lattices with *r/a*=0.32 and 0.41, respectively. The curves in c) represent the transmission spectra for different pillar heights *h*. b) and d) are simulated acoustic pressure distributions showing the topological edge states in perfect lattice and lattice with defects, respectively.

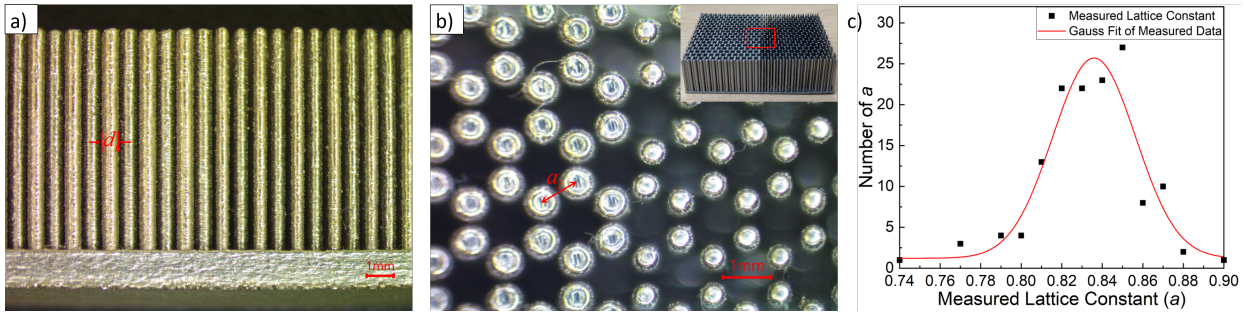

FIG. 3. a) Side view image of the metal topological waveguide under the optical microscope. b) Top view image of the metal topological waveguide under the optical microscope. The a_i is the distance between the nearest two metal pillars, corresponding to the lattice constant of the phononic crystal. c) Distribution of the measured lattice constants fit to a Gaussian distribution.

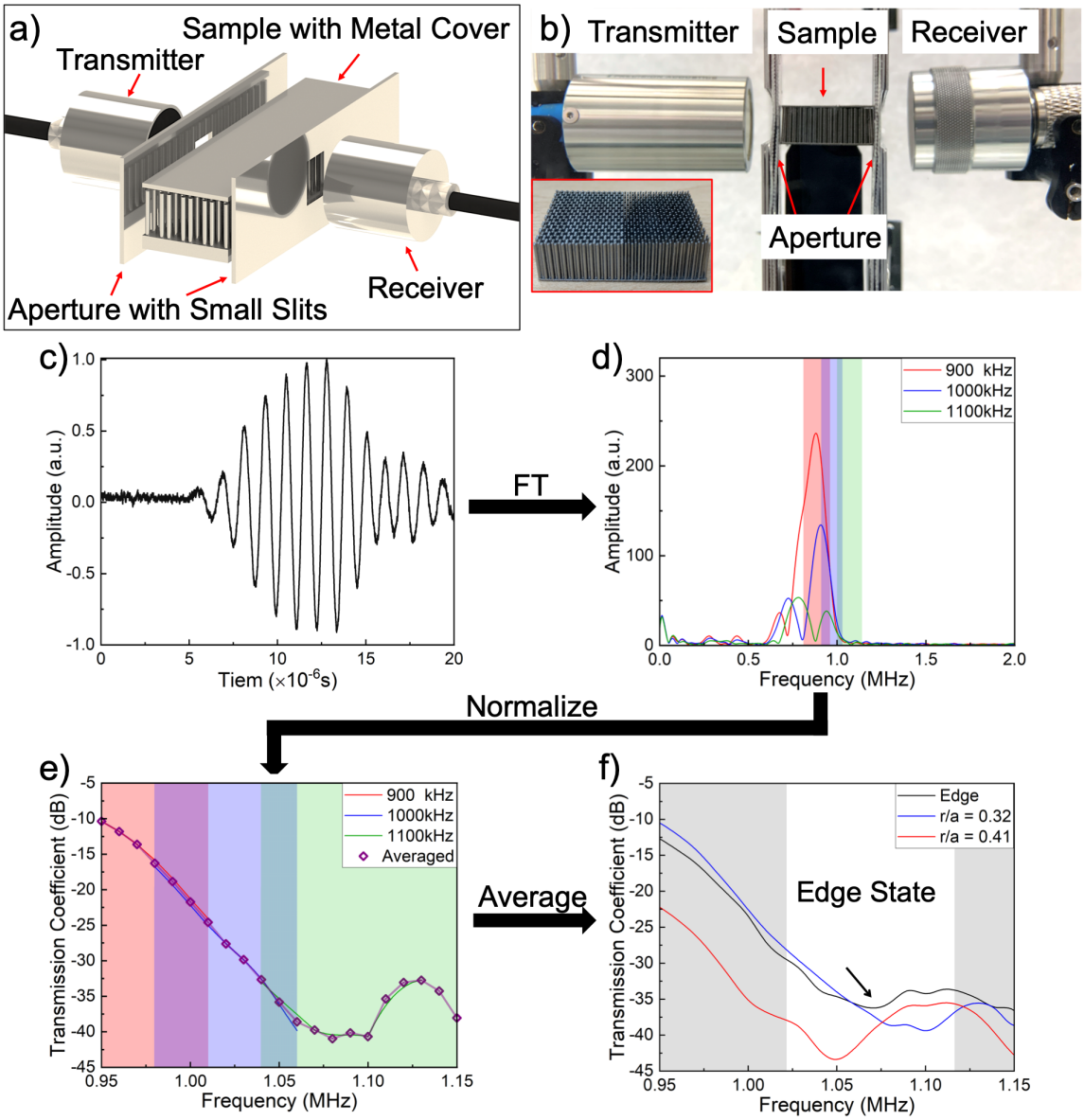

FIG. 4. a) and b) The schematic and a picture of the experimental setup. The transmitter, metalic apertures with small slits, the sample and the receiver are aligned along one axis. c) An example of a measured time domain transmitted signals through the topological lattice. d) Frequency spectra of transmitted signals through the topological lattice corresponding to emitted pulse center frequency of $f_c = 0.9, 1$, and 1.1 MHz before being normalized by the transmission spectra through water. The shaded areas correspond to the spectrum sections between the FWHM points of each measurement. e) The normalized transmission coefficient spectra of one set of measurement with *r/a*=0.32. f) Final transmission spectra of the trivial lattice with *r/a*=0.41, topological lattice with *r/a*=0.32, and the topological edge state through the waveguide with relatively high transmission.